Influence of coarse-graining parameters on the analysis of DEM simulation results

Thomas Weinhart, Stefan Luding

Multiscale Mechanics (CTW & MESA+), University of Twente,
P.O. Box 217, 7500AE Enschede, Netherlands

Carlos Labra, Jin Y. Ooi

Institute for Infrastructure & Environment, School of Engineering,
University of Edinburgh, UK

Abstract

The discrete element method is used extensively for the simulation of granular materials. The great majority of engineering applications require bulk design parameters to be determined which requires some averaging or coarse graining techniques to be applied to the particle data from DEM computations. Although numerous papers have been published on these techniques, we suggest that there are still significant challenges in the calculation of the continuum quantities from the particle data. This is chiefly because DEM computes at grain contact level and at small computational time steps, whereas important engineering events often occur at much larger timescale, so the question of what temporal and spatial averaging scales should be adopted is not so clear. This work outlines the analysis of the influence of the different parameters used in the coarse graining methods for the projection of discrete quantities into continuum fields.

A silo flow model with internal flow pattern is used as a test case, where there is stagnant zone, high shear localization zone and a fast core flow zone. This allows one to study the influence of the averaging length scale and the temporal scale for the spatial-temporal averaging, and their relationship with other model parameters as the sampling frequency and simulation time.

Email address: `email@uni.edu` (Thomas Weinhart)

1. Introduction

Granular systems, conglomerations of individual particles, are everywhere in both industrial and natural settings, from pharmaceutics, mining and handling of resources and food processing to hazard prediction for landslides or earthquakes. The Discrete Element Method (DEM) is a powerful computational tool to study such systems; the method allows the simulation of tens of millions of individual particles by solving Newton's laws for each particle. To visualise and analyse the granular system, local macroscopic quantities such as density, velocity and stress can be extracted from the discrete simulation data (particle positions and velocities, interaction forces and torques).

Several micro-macro transition techniques have been developed to calculate continuum fields, as shown in [1]. Particularly the stress tensor is of interest: the techniques include the Irvin-Kirkwood approach [2, 3], which allows the calculation of the stress tensor within small volumes or bins, or the method of planes [4]. Here, we use the coarse-graining approach (CG) as described in [5, 6]. The comparison between the latter two approaches can be found in [7].

The CG method [5, 6] has several advantages over other methods, including: *i)* the fields automatically satisfy the conservation equations of continuum mechanics, even for single particles (no ensemble averaging is required), and *ii)* it is not assumed that the particles are rigid or spherical. The only assumptions are: each particle pair has a single point of contact, the contact area can be replaced by a contact point, and collisions are not instantaneous. CG has been successfully applied to both granular [8] and molecular flows [9].

Note that the word 'coarse-graining' is ambiguous: In molecular dynamics, coarse-graining consists of replacing an atomistic description of a molecule with a lower-resolution coarse-grained model that averages over the fine details. It is also used as a synonym for homogenisation methods or the micro-macro transition. Here, we apply it to the specific micro-macro transition method developed

2

in [5, 6].

Coarse-graining involves a spatial scale, w, and, when temporal coarse-graining is applied, a temporal scale Δt as well. For very small scales, the resulting fields can be strongly fluctuate due to insufficient amount of data at each point; for very large scales, the fields become scale-dependent due to macroscopic gradients; for appropriately large scales (and a sufficient amount of data), the field values plateau to scale-independent values [10].

The spatial CG scale was studied in detail in [11] for steady granular chute flows. Two distinct coarse-graining length scale ranges were identified, where the fields are almost w-independent. The smaller, sub-particle length scale, $w \ll d$, resolves details on the particle scale, such as the density and shear rate fluctuations between particle layers. The larger, particle scale, $w \approx d$, leads to bulk stress, velocity, and density fields in which particle-scale effects are averaged out, and is thus appropriate to study the macroscopic behaviour. However these findings only applies to steady state flow condition and may not be valid for other conditions.

Spatial coarse-graining, however, is often not sufficient to obtain well-defined macroscopic fields, as the fields can show strong fluctuations over time: In these cases, temporal coarse-graining is applied, usually by averaging the data over a time interval Δt. While Δt can be arbitrary large in steady situations, it is unclear how to choose the temporal scale in dynamic situations.

In this study, the technique is applied for the analysis of a silo flow model with internal flow pattern for the study of the influence of the spatial coarse-graining parameter. As the silo flow is slowly changing with time, the temporal scale is investigated as well. We begin by reviewing the spatial coarse-graining approach in §2. Then the silo flow model is introduced in §3. In §4, the CG approach is then applied to the silo flow and the resulting field are used to define the flow regions and determine the flow rheology in the shear band.
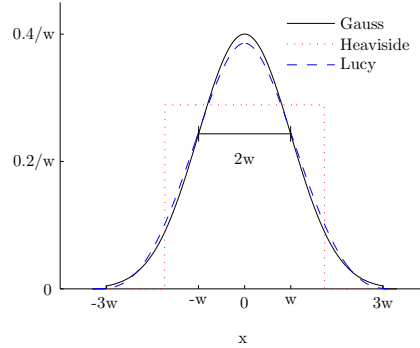
Figure 1: Coarse-graining functions for one space dimension. The cutoffs for Heaviside and Lucy are chosen as $c = \sqrt{3}w$ and $c = \sqrt{11.5}w$, respectively, such that w equals the standard deviation for all three functions.

2. Statistics

To extract the macroscopic fields, we use the spatial coarse-graining approach as detailed in Weinhart *et al.* [8, 12] and references therein, which will be reviewed in this section.

It is assumed that collisions are not instantaneous, that each particle pair has at most one contact area, and that each contact area is small enough that it can be replaced by a single contact point. Thus, the evolution of the system is described by evaluating Newton's law of motion, where the force $\vec{f}_i$ and torque $\vec{t}_i$ acting on particle i is given by the body force $\vec{f}_i^{\mathrm{b}}$ and the interaction forces $\vec{f}_{ij}$ and torques $\vec{t}_{ij}$ with other particles and walls,

$$\vec{f}_i = \vec{f}_i^{\mathrm{b}} + \sum_{j=1}^{N+N_b} \vec{f}_{ij}, \quad \vec{t}_i = \sum_{j=1}^{N+N_b} \vec{t}_{ij} + (\vec{c}_{ij} - \vec{r}_i) \times \vec{f}_{ij}, \tag{1}$$

Here, particles are labeled from 1 to N, while walls are labeled from $N + 1$ to $N + N_b$, $\vec{r}_i$ is the centre of mass of particle i and $\vec{c}_{ij}$ is the contact point between particles i and j.

2.1. Mass density and velocity

In statistical mechanics, it is assumed that each particle's mass is located at its centre. Thus, the microscopic (point) mass density, ρ^{mic}, at a point $\mathbf{r}$ at time

4

t is defined by

$$\rho^{\mathrm{mic}}(\mathbf{r}, t) = \sum_{i=1}^{N} m\delta\left(\mathbf{r} - \mathbf{r}_i(t)\right), \qquad (2)$$

where $\delta(\mathbf{r})$ is the Dirac delta function.

A macroscopic mass density field can then be extracted by convoluting the microscopic mass density with a coarse-graining function $\mathcal{W}(\mathbf{r})$, which yields

$$\rho(\mathbf{r}, t) = \int_{\mathbb{R}^D} \rho^{\mathrm{mic}}(\mathbf{r}', t)\mathcal{W}\left(\mathbf{r}'\right) d\mathbf{r}' = \sum_{i=1}^{N} m\mathcal{W}\left(\mathbf{r} - \mathbf{r}_i(t)\right), \qquad (3)$$

with D the number of spatial dimensions.

A cut-off Gaussian coarse-graining function is used,

$$\mathcal{W}(\mathbf{r}) = V_\omega^{-1} \exp\left(-\frac{r^2}{2\omega^2}\right), \text{ if } r := |\mathbf{r}| < c, \, 0 \text{ else}, \qquad (4)$$

with coarse-graining width $w > 0$ and cutoff $c = 3w$. The constant V_ω is chosen such that the integral over the coarse-graining function is unity,[1]

$$\int_{\mathbb{R}^D} \mathcal{W}(\mathbf{r})\, d\mathbf{r} = 1, \qquad (5)$$

which is required such that the integral over the density equals the total mass.

The Gaussian function is chosen as it delivers smooth results; the cut-off is applied to limit the computational expense. However, other coarse-graining functions are possible, such as Heaviside or Lucy polynomials (see figure 1), as long as they satisfy equation (5). The resulting coarse-grained fields depend only weakly on the choice of the coarse-graining function, but the standard deviation of the coarse graining function $\sigma_{\mathcal{W}} \approx \sqrt{D}w$ is the key parameter [6, 13, 11].

Similarly, the coarse-grained momentum density vector $\mathbf{p}(\mathbf{r}, t)$ is given by

$$\mathbf{p}(\mathbf{r}, t) = \sum_{i=1}^{N} m\mathbf{v}_i \mathcal{W}(\mathbf{r} - \mathbf{r}_i), \qquad (6)$$

where $\mathbf{v}_i$ is the velocity of particle i. The macroscopic velocity field $\mathbf{V}(\mathbf{r}, t)$ is then defined as the ratio of momentum density and mass density fields,

$$\mathbf{V}(\mathbf{r}, t) = \mathbf{p}(\mathbf{r}, t)/\rho(\mathbf{r}, t). \qquad (7)$$

---

[1] For three spatial dimensions, $V_\omega = \mathrm{erf}(\frac{c}{\sqrt{2}w}) - \sqrt{\frac{2}{\pi}}\frac{c}{w}\exp(\frac{-c^2}{2w^2})$, and $\approx \sqrt{3}w$ is the standard deviation.

2.2. Stress

Next, we consider the momentum conservation equation with the aim of establishing the macroscopic stress field, $\sigma_{\alpha\beta}$. We split the stress

$$\boldsymbol{\sigma} = \boldsymbol{\sigma}^k + \boldsymbol{\sigma}^c, \tag{8a}$$

into its kinetic ($\boldsymbol{\sigma}^k$) and contact ($\boldsymbol{\sigma}^k$) contributions

$$\boldsymbol{\sigma}^k = \sum_{i=1}^{N} m \mathbf{V}_i' \mathbf{V}_i' \mathcal{W}(\mathbf{r} - \mathbf{r}_i), \tag{8b}$$

$$\boldsymbol{\sigma}^c = \sum_{i=1}^{N} \sum_{j=i+1}^{N} \mathbf{f}_{ij} \mathbf{r}_{ij} \int_0^1 \mathcal{W}(\mathbf{r} - \mathbf{r}_i + s\mathbf{r}_{ij}) \, \mathrm{d}s \tag{8c}$$

$$+ \sum_{i=1}^{N} \sum_{k=N+1}^{N+N_b} \mathbf{f}_{ik} \mathbf{a}_{ik} \int_0^1 \mathcal{W}(\mathbf{r} - \mathbf{r}_i + s\mathbf{a}_{ik}) \, \mathrm{d}s, \tag{8d}$$

with interaction forces $\mathbf{f}_{ij} = -\mathbf{f}_{ji}$, branch vectors $\mathbf{r}_{ij} = \mathbf{r}_i - \mathbf{r}_j$, and contact-to-centre vectors $\mathbf{a}_{ik} = \mathbf{r}_i - \mathbf{c}_{ik}$, where $\mathbf{c}_{ik}$ denotes the contact point between the particle i and wall k. Further,

$$\mathbf{V}_i'(\mathbf{r}, t) = \mathbf{v}_i(t) - \mathbf{V}(\mathbf{r}, t). \tag{9}$$

is the fluctuation velocity field of particle i. Note that this definition of the fluctuation velocity is scale dependent for $w > 0.1d$, thus even for small spatial scales, as discussed in [14, 11]. Furthermore, the boundary interaction force density is introduced

$$\mathbf{t} = \sum_{i=1}^{N} \sum_{k=N+1}^{N+N_b} \mathbf{f}_{ki} \mathcal{W}(\mathbf{r} - \mathbf{c}_{ik}), \tag{10}$$

which is a measure of the force the particles exert on the wall and has nonzero values only near the walls.

By design, these newly defined fields satisfy exactly the continuity and momentum equations [6, 12]

$$\partial_t \rho + \nabla \cdot \rho \vec{\mathbf{V}} = 0, \tag{11a}$$

$$\partial_t (\rho \mathbf{V}) + \nabla \cdot (\rho \mathbf{V} \mathbf{V}) = \nabla \cdot \boldsymbol{\sigma} + \rho g - \mathbf{t}. \tag{11b}$$

where the short notation $\partial_t = \partial/\partial t$ is used.

6

2.3. Averaging over time and spatial dimensions

Further, time-averaging can be applied to decrease temporal fluctuations. For that, a uniform distribution function is used,

$$\langle \rho \rangle_t = \frac{1}{\Delta t} \int_{t-\Delta t/2}^{t+\Delta t/2} \rho(\mathbf{r}, t) \, \mathrm{d}t. \tag{12}$$

In steady situations, the fields are homogeneous in time and thus time averaging interval can be arbitrarily large. For unsteady situations, however, the average value becomes scale-dependent, and time averaging can only be applied over a sufficiently small interval, as we will investigate further in this paper.

Similarly, the continuum fields can be averaged over the spatial directions in which the flow is homogeneous. This will be denoted by angled brackets; *e.g.*, the average of ρ over the y-direction is given by

$$\langle \rho \rangle_y (x, z, t) = \frac{1}{y_1 - y_0} \int_{\mathbb{R}} \rho(\mathbf{r}, t) \, \mathrm{d}y, \tag{13}$$

where $[y_0, y_1] = [0, 4]$cm denotes the size of the domain. The integration is applied over the whole domain to capture the tails of the CG functions, which sometimes extend beyond the domain. To save computation effort and to accurately resolve the integral, this averaging is done analytically by applying the integral to the coarse graining function directly, *i.e.*

$$\langle \rho \rangle_y (x, z, t) = \sum_{i=1}^{N} m_i \langle \mathcal{W} \rangle_y (x - x_i, z - z_i, t). \tag{14}$$

The averaged velocity is then evaluated as

$$\langle \mathbf{V} \rangle_y = \langle \mathbf{p} \rangle_y / \langle \rho \rangle_y. \tag{15}$$

In Ref. [15] it is shown that the averaged fields still satisfy the mass and momentum equations, if the averaging is applied in directions where the flow is homogeneous, and/or if the averaging is carried out over (*i*) all the direction from $-\infty$ to ∞ or (*ii*) via periodic boundary conditions.

3. DEM modelling of silo flow

Over the last decade, DEM has been increasingly used to model many granular flow situations involving complex flow patterns that evolve spatially and temporally. In this type of problems, spatial and temporal averaging take an important role in the analysis of the results. Here a DEM model of flow from a flat-bottomed silo has been specifically chosen to study the influence of the spatial and temporal coarse-graining parameters. With a central outlet through the flat bottom, an internal flow channel develops and evolves over time providing a rich phenomenological ground for this study.

The flow consists of three distinct zones: A stagnant zone near the side walls, a zone with high localized shear and a fast core flow zone in the middle of the silo.

The geometry of the silo model is presented in Figure 2. Periodic boundary conditions are applied in y-direction, such that the flow is homogeneous in y.
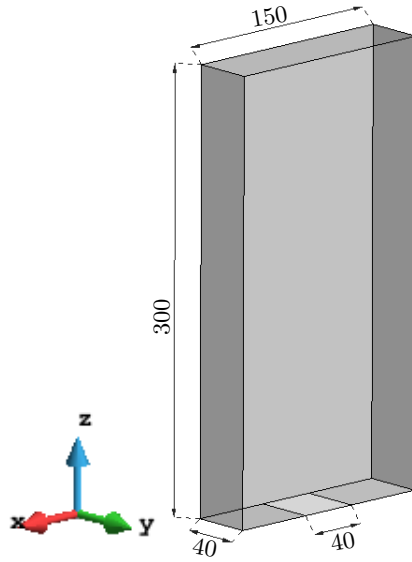
Figure 2: Silo geometry (in mm). Dark grey area denotes walls, the light grey area at the base denotes the outflow. The system is periodic in y-direction.

The model considers 56 241 non-spherical monodisperse particles. Each par-

ticle is created with two overlapping spheres with centre-centre distance $0.25d_s$, where d_s is the diameter of the contituent spheres, as shown in Figure 3. For the purpose of the present study, the particle size d is defined as the diameter of the volume-equivalent sphere ($d = 3.33$ mm).
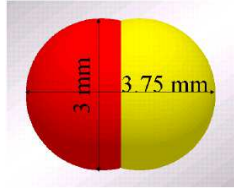
Figure 3: Particle shape.

The Hertz-Mindlin contact model implemented in EDEM® [16] is used, with the material properties of the particles: mass density of 950 kg/m^3; shear modulus of 0.1 GPa; Poisson's ratio 0.4. The material properties of the walls are: shear modulus 10 GPa and Poisson's ratio 0.2. The contact model parameters for the particle-particle interaction considers a friction coefficient 0.577. and for the particle-wall interaction a friction coefficient 0.5 is used. The coefficient of restitution is set to 10^{-4}, but does not have influence in the flow patterns. The Relative Velocity Dependent (RVD) rolling friction model [17] is used with a rolling friction coefficient 0.2. The total simulation time is 2.5 s, with a time step of 1.54 μs and a sampling frequency of 200 Hz.

4. Results

Static, sheared, and fast-flowing zones: Figure 4 shows the evolution of the particle flow in the silo. The particles are stationary as long as the outlet is closed, *i.e.* $t < 0.1$ s. After the outlet is opened, particles begin to flow out as flow regime begins to propagate upwards and a nearly steady flow begins to develop in the centre of the silo; the outflow rate is steady for $t > 0.6$ s. The particles near the side walls remain static; this static zone slowly decreases in size as the silo is emptied. To study the typical flow behaviour, we investigate

9

the flow at $t = 1.2\,$s, where the flow is fully developed and 2/3 of the initial particles still remain in the silo.

(a) t=0.745s   (b) t=1.200s   (c) t=1.490s   (d) t=2.240s
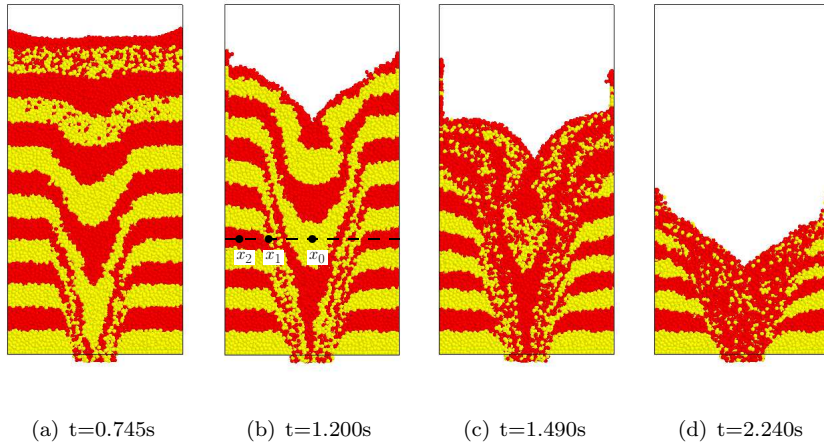
Figure 4: Silo flow evolution.

We can clearly distinguish three zones: *(i)* a stagnant zone near the side and bottom wall, *(ii)* a zone of high shear localization, and *(iii)* a fast-flowing core. To study these zones further, we select three points at horizontal positions $x_0 = 0$ cm, $x_1 = -3.75$ cm, $x_2 = -6.25$ cm and at height $z = 10$ cm, one from each zone, to be investigated in detail (see figure 4).

4.1. Averaging over the depth y

Next, we average over the directions, in which the macroscopic fields are homogeneous. This is the case in the y-direction, in which the domain is periodic and uniform. We observe that the variations of solid fraction, momentum and stress in the y-direction are smaller than the standard deviation (not shown). Thus, all results shown here are averaged over the y-direction.

4.2. Homogeneity in time

To determine an appropriate averaging time interval $[t - \frac{\Delta t}{2}, t + \frac{\Delta t}{2}]$, we plot the profiles of instantaneous solid fraction, momentum and downward stress over time at x_0, x_1, and x_2 in Figure 5. After the silo exit is opened, the velocity

10

rapidly increases before settling to a nearly constant rate for $0.75\,\text{s} < t < 2\,\text{s}$. During this time interval, all profiles are nearly constant in time in the flowing core (x_0) and the shear zone (x_1). In the static zone (x_2), the stress decreases over time, as the silo is emptied, and consequently the solid fraction decreases slightly.
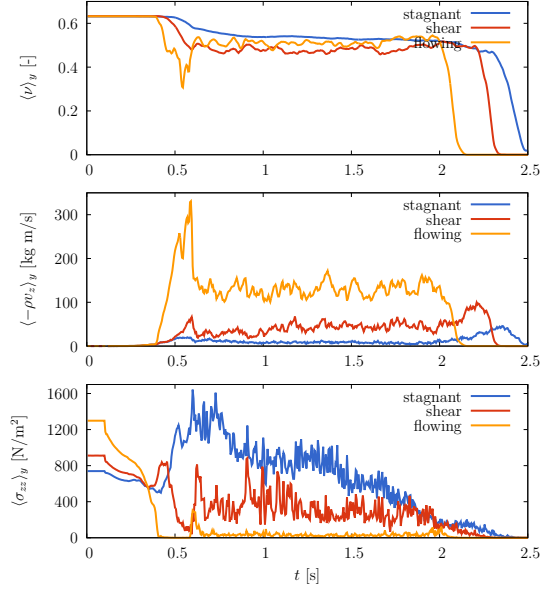
Figure 5: Instantaneous solid fraction, momentum and stress profile in the flowing (x_0), shear (x_1) and stagnant (x_2) zone at height $z = 10\,\text{cm}$, averaged over y, with $w = d$.

In figure 6, the dependence on Δt of the averaged solid fraction, momentum and downward stress is presented. The averaged variables in the figures present stable values for the stagnant and flowing zones for Δt of up to 1.5s. However, the shear zone presents a degree of variation especially for the solid fraction, with a lower variation with $\Delta t < 1\,\text{s}$ and increasing for higher values of Δt. This can be explained by the displacement of the shear band during the discharge. For large values of Δt, the spatial average in the shear zone (x_1) captures particles out of the shear band, where the solid fraction is higher. The same occurs within the stagnant zone (x_2), where part of the shear band and the initial conditions is captured for $t > 1.8\,\text{s}$.
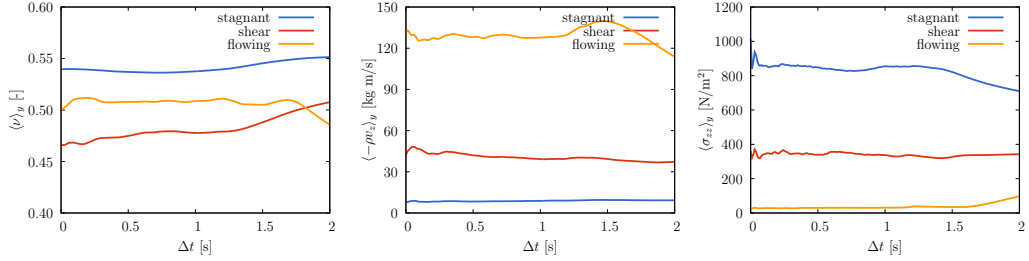
Figure 6: Dependence on Δt of solid fraction (left), momentum (centre) and stress (right) at flowing (x_0), shear (x_1) and stagnant (x_2) zone, with $w = d$ and $t = 1.2\,\text{s}$, averaged over y.

The variation for high values of Δt can be observed in a better way using the coefficient of variation (CV) of the averaged variables, as presented in figure 7.

For all three variables, the CV increases gradually until $\Delta t = 0.5\,\text{s}$, then is nearly stable for $0.5\,\text{s} < \Delta t \le 1.1\,\text{s}$. For higher Δts, the CV of the averaged variables starts to increase, as we average over an interval that includes a significant share of non-steady flow, which occurs before $t < 0.75\,\text{s}$. For $\Delta t \le 1.1\,\text{s}$, the CV of solid fraction is negligible (< 0.02), as it does not vary strongly in time. The CV of momentum is larger, but varies within a narrow range (0.1 in the flowing zone and 0.2 at the shear and static zones), and the same holds for the stress in the flowing and shear zone (0.4). In the stagnant zone, however the CV of stress (and solid fraction) show a gradual increase for $\Delta t > 0.5$, as these variables strongly vary within this interval, as shown in figure 5. This means the chosen time interval should be smaller than $0.5\,\text{s}$.

To select the time interval, the combination with the coarse-graining width (w) must be considered. In the following section the dependence between both parameters is analysed.

4.3. Dependence on the coarse-graining width

In order to obtain an accurate representation of the coarse-grained variables, appropriate choices for the time-averaging interval and the coarse-graining width are required. To determine the appropriate coarse-graining width we plot the comparison of the spatio-temporally averaged solid fraction (figure 8), momentum (figure 9) and downward stress (figure 10) for the three sample points with
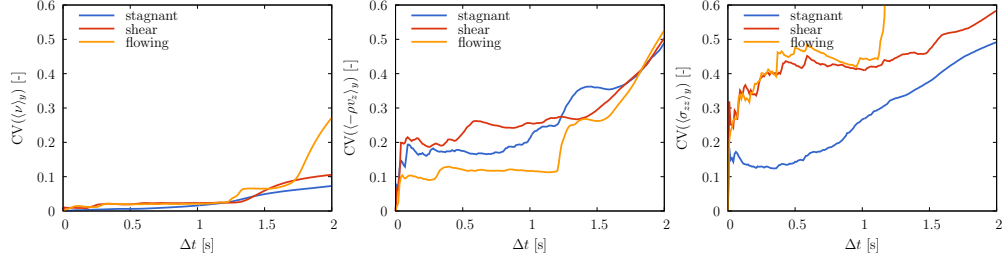
Figure 7: Coefficient of variation of Δt in averaged over y of solid fraction (left), momentum (centre) and stress (right) at flowing (x_0), shear (x_1), and stagnant (x_2) zone, with $w = d$ and $t = 1.2\,\mathrm{s}$.

different values of the coarse-graining width and time intervals.

In figure 8 an important influence of Δt and w in the solid fraction is found for $w/d < 0.5$, where the computed solid fraction is independent of the range of temporal and spatial scale chosen. For w/d¿1.5, the solid fraction starts to change in the stagnant and shear zone. For the flowing core, the time averaged and instantaneous solid fraction differs for low values of w/d, but converges to a stable value for $w/d \geq 1.5$.
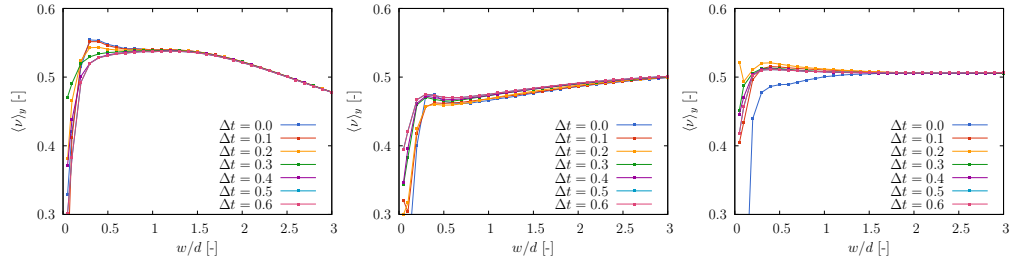
Figure 8: Dependence of solid fraction on w and Δt in the stagnant (left), shear (centre) and flowing (right) zone (centred at t=1.2s, averaged over the depth y).

A similar influence of w/d is found for the momentum (figure 9). In this case the influence on the time interval is higher, particularly in the flowing (x_0) and shear (x_1) zones. A noticeable exception is again the instantaneous case ($\Delta t = 0$) which deviates significantly from the others.

For the stress (figure 10), a clear plateau is found between $0.5 < w/d < 1.0$
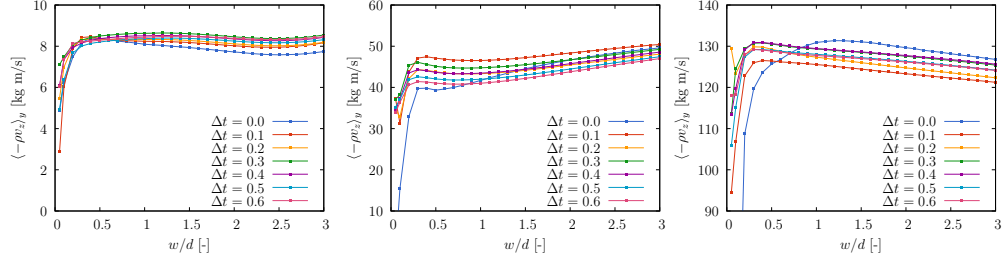
Figure 9: Dependence of momentum on w and Δt in the stagnant (left), shear (centre) and flowing (right) zone (centred at t=1.2s, averaged over the depth y).

for the stagnant zone (x_2), where a low influence of Δt is seen. For the flowing core (x_0) and shear zone (x_1), the influence of Δt is not significant for $w/d > 0.5$, whilst a high variation of the value with w is found. This contrasts with the relatively stable solid fraction with the temporal and spatial scales, revealing the nature of the problem that whilst solid friction may remain relatively constant in the shear and core flowing zones in a silo, the stress regimes can vary much more. Again the instantaneous case $(\Delta t = 0)$ deviates significantly from the others which suggests that computing DEM results using an instantaneous snapshot can lead to erroneous result.
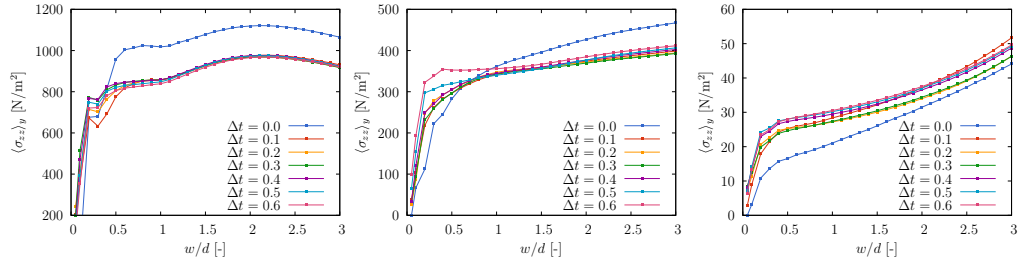
Figure 10: Dependence of stress on w and Δt in the stagnant (left), shear (centre) and flowing (right) zone (centred at t=1.2s, averaged over the depth y).

Based in the previous results, the range of $0.5 < w/d < 1.5$ appears to be the most favourable w/d values to use. Similar plateaus in the coarse-graining width w/d have been observed in [18, 10, 11, 19] , as discussed in the introduction. Thus, the coarse-grained fields are scale independent for $w = d$. For this spatial scale, it was shown in §4.2 that time-averaging shows that the variables are

14

independent of the chosen time interval for $\Delta t < 1.2\,\mathrm{s}$. However, the variance of the time-dependent stress in the stagnant zone increases for $\Delta t > 0.4\,\mathrm{s}$ (figure 7). Therefore $\Delta t = 0.4\,\mathrm{s}$ is selected as the optimal time-averaging interval for this problem.

After the temporal and spatial averaging parameters are thus chosen, the coarse-graining technique is used to study the flow pattern in the model as presented in the following sections.

4.4. Shear band study

Three zones: First, we study the profiles of solid fraction (packing density), velocity, and shear rate, plotted in figure 11. The fields are averaged in depth y and over a small time interval $1\,\mathrm{s} < t < 1.4\,\mathrm{s}$ and a coarse-graining width of $w = d$ is used, as justified above. A resolution of 100×60 points in x and z is chosen to resolve the data spatially. We can clearly distinguish some key features of the three zones: *(i)* a stagnant zone near the side and bottom walls, where the density is high, the velocity nearly vanishes, and the stress increases with height, as expected from a hydrostatic stress profile (figure 16); *(ii)* a zone of high shear localization, combined with a low density (due to dilatancy) and moderately large stresses; and *(iii)* a fast flowing core, in which the velocity is high, but with small shear rates and lower stresses.
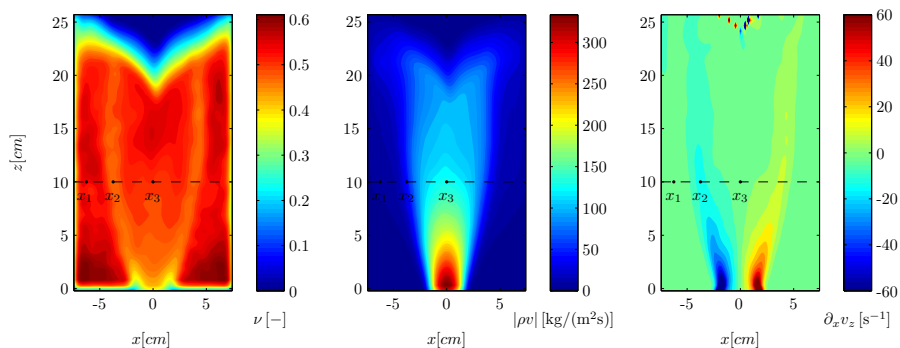
Figure 11: Profile of solid fraction ν (left), momentum $|\rho v|$ (centre), and horizontal shear rate $\partial_x v_z$ (right), averaged over y and $1.0\,\mathrm{s} < t < 1.4\,\mathrm{s}$ with $w = d$. The three points shown as x_1, x_2, x_3 in the plot as well as the profile at $z = 10$ cm, are selected for further analysis.

15
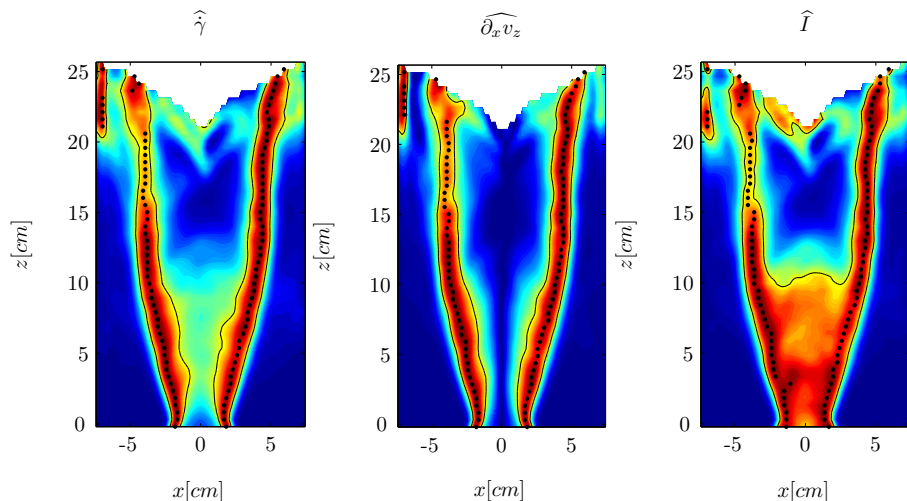
Figure 12: Tensorial shear rate $\dot{\gamma}$, horizontal shear rate $\partial_x v_z$, and inertial number $I = \frac{\dot{\gamma} d}{\sqrt{p/\rho_p}}$ scaled onto the interval $[0, 1]$ by its maximum at each height, see (16). Data for $\nu < 0.1$ (white area on the top) is not considered. Dots denote the maxima of the depicted values in the left and right half of the domain, black contours denote demarcation of the shear band where the scaled value is less than a tolerance ($tol = 0.6$). All values averaged over y and $1 \leq t \leq 1.4$ for $w = d$.

Shear band: In order to study the shear band in more detail, *i.e.* the zone between the static and the flowing region of the granulate, we attempt to define the location of its centre and width. In figure 12 we show three attempts to define this zone, using (a) the tensorial shear rate $\dot{\gamma} = \frac{1}{2}\sqrt{(\partial_x v_z + \partial_z v_x)^2 + (\partial_x v_x - \partial_z v_z)^2}$, (b) the horizontal shear rate $\partial_x v_z$, and (c) the inertial number $I = \frac{\dot{\gamma} d}{\sqrt{p/\rho_p}}$, which is the tensorial shear rate scaled by the pressure p, particle size d and density ρ_p. As the shear rate is rapidly decreasing in height, we scale each quantity by its maximum at each height z, which is denoted by the hat operator,

$$\hat{.}(x, z) := \frac{.(x, z)}{\max_x .(x, z)}. \tag{16}$$

While the tensorial shear rate definition is sensitive to both pure and simple shear, the horizontal shear rate does not take pure shear into account. Thus, both definitions show non-zero values in the shear band (where simple shear is active), but the horizontal shear rate vanishes in the lower part of the fast-flowing core, where the width of the core region contracts towards the orifice,

16

causing pure shear.

At first, we define the location of the left and right shear bands, $C_l(z)$ and $C_r(z)$, by the maxima of each quantity in the left ($x \leq 0$) and right half ($x \geq 0$) of the domain; the resulting shear band locations are similar for all three definitions. Next, we define the shear band as all values for which each scaled quantity is larger than a given tolerance, which we choose here to be 0.6 (with 1 being the maximum), shown demarcated by the solid lines in figure 12. Here, we see clear differences between the three definitions: The scaled horizontal shear rate is only larger than 0.6 in a tight region around the centre of the shear band, giving a good definition of the shear band throughout the silo. This is also true for the tensorial shear rate; however, the large values in the lower region of the flowing zone decreases the quality of the shear band definition. This undesired effect is intensified if we consider the inertial number, as the pressure p in the lower flowing zone is much lower than in the shear band, thus increasing the inertial number there. Therefore we choose to use the horizontal shear rate $\partial_x v_z$ for the shear band definition.
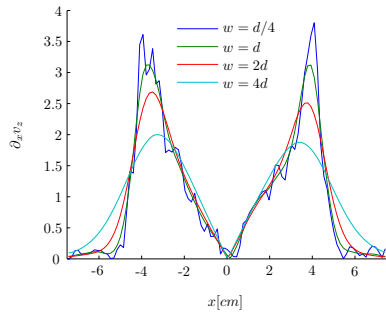
Figure 13: Horizontal shear rate $\partial_x v_z$ at $z = 0.1\,\mathrm{cm}$ averaged over y and $1.0\,\mathrm{s} < t < 1.4\,\mathrm{s}$ for varying coarse graining width w.
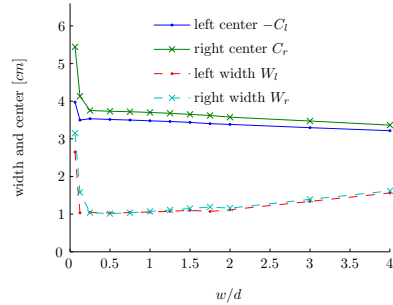
Figure 14: centre and width of the left and right shear band at $z = 0.1\,\mathrm{cm}$ for varying w.

Defining the shear band centre as the location of the maximum (figure 12) has two disadvantages: Firstly, as the grid resolution is finite (100 points in x-direction), the centre of the shear band can only be located with an accuracy of $0.15\,\mathrm{cm}$, resulting in an undesirable stepwise definition. Secondly, the shear

17
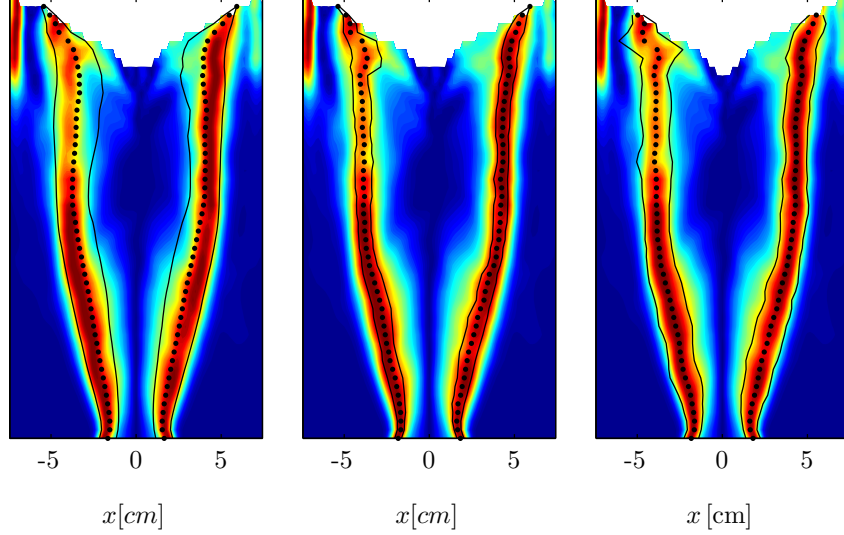
Figure 15: Fits of the shear band based on (17) for all values (left) and for $\widehat{\partial_x v_z} > 0.6$ (centre), as well as a Gaussian fit to (18) (right).

band splits into several arms for small w, as the larger noise in the data can create local maxima of the shear rate far from the shear band, see figure 13. To avoid these effects, two other definitions were tested, as shown in figure 15: Firstly, the centres and widths of the shear bands are defined as the centroids and the hygroscopic radius in the left and right half plane, respectively, with $\partial_x v_z$ acting as the mass,

$$C_l(z) = \frac{\int_{x_0}^0 \partial_x v_z\, x\, dx}{\int_{x_0}^0 \partial_x v_z\, dx}, \quad W_l(z) = \sqrt{\frac{\int_{x_0}^0 \partial_x v_z (x - C_l)^2\, dx}{\int_{x_0}^0 \partial_x v_z\, dx}}, \qquad (17a)$$

$$C_r(z) = \frac{\int_0^{x_1} \partial_x v_z\, x\, dx}{\int_0^{x_1} \partial_x v_z\, dx}, \quad W_r(z) = \sqrt{\frac{\int_0^{x_1} \partial_x v_z (x - C_r)^2\, dx}{\int_0^{x_1} \partial_x v_z\, dx}}. \qquad (17b)$$

This produces a smooth definition of the shear band. The centre of the shear band, however, is badly approximated, as the shear band is asymmetric, with the peak shear rate close to the outer boundary of the shear band. Therefore, a second fit was obtained by only considering values for which $\widehat{\partial_x v_z}$ is above $tol = 0.6$, producing a good approximation of the shear band; however, the

18

width of the shear band is now dependent on the choice of *tol*.

Therefore, a forth definition of the shear band was chosen, where the centre and width shear band was defined by fitting $\partial_x v_z$ by a Gaussian function with the least squares approximation

$$\min_{C_l, W_l, M_l} \int_{x \leq 0 \cap \widehat{\partial_x v_z} > tol} \left| \partial_x v_z(x, z) - M_l \exp\left(-\frac{(x - C_l)^2}{2W_l^2} \right) \right|^2 dx \qquad (18a)$$

$$\min_{C_r, W_r, M_r} \int_{x \geq 0 \cap \widehat{\partial_x v_z} > tol} \left| \partial_x v_z(x, z) - M_r \exp\left(-\frac{(x - C_r)^2}{2W_r^2} \right) \right|^2 dx, \qquad (18b)$$

As the shear band is not symmetric, we again only consider values for which $\widehat{\partial_x v_z} > tol = 0.6$; for this definition, however, the shear band width is independent of the choice of *tol* for *tol* > 0.5.

To show that the shear band is now well-defined, the centre and width location of the shear band is plotted for varying coarse-graining widths w in figure 14. We observe that the both the shear band centre and band width are nearly stable for $0.2 < w/d < 2$, with the centre of the band moving slightly away from the central axis as w decreases, probably because of a varying shear gradient in the region.

4.5. Stress analysis

Stress anisotropy: To study the behaviour of the stress, we plot the normal stresses as well as the shear stress σ_{xz} in figure 16. This represents the complete description of the stress, as the remaining shear stress components are fluctuating around zero and the stress tensor is nearly symmetric. We observe that the normal stress components differ strongly from each other, with the stress in downward direction, σ_{zz}, being highest and the lateral stress, σ_{xx} the weakest. The stresses in the static zone are the highest stresses and increase with depth, which indicates that they are governed by the weight of the solid and the friction on the wall. An arch of higher normal stress σ_{xx} extends through the flowing zone from the top of the static zone (best seen in the σ_{xx} plot in figure 16), thus allowing the flow below the arch to flow at lower pressure.

Stress balance: If we average the third momentum balance equation (11b) over x, y and $t \in [1, 1.4]$ s and assume that the rate of change in momentum is
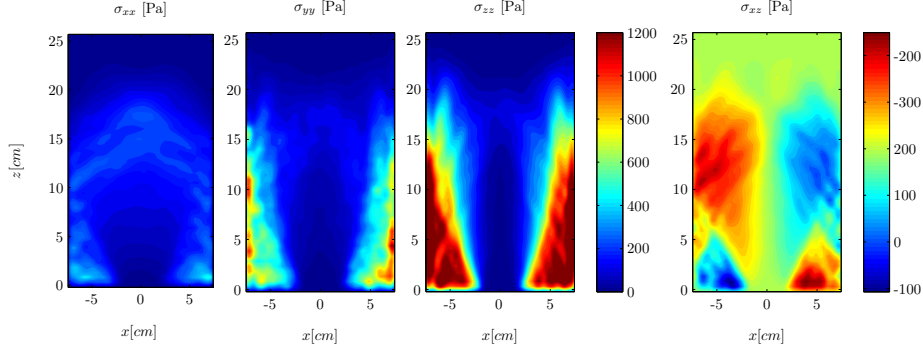
Figure 16: Profiles of normal and shear stress components, averaged over y and $1.0\,\mathrm{s} < t < 1.4\,\mathrm{s}$ with $w = d$.

negligible, we obtain a balance between the weight of the flow, the downward normal stress and the force acting on the walls,

$$g_z \langle \rho \rangle_{xyt} = -\partial_z \langle \sigma_{zz} \rho \rangle_{xyt} - \langle t_z \rangle_{xyt}. \tag{19}$$

This is shown to be valid in Figure 17. We can further split the wall interaction force density $\mathbf{t}$ into three components $\mathbf{t} = \mathbf{t}^l + \mathbf{t}^r + \mathbf{t}^b$, which denote the forces on the left and right side wall and the bottom wall, respectively. Averaging further over z, we obtain that $(t_z^l + t_z^r)/t_z = 21\%$ of the flow weight is held by the shear forces on the side walls, while $t_z^b/t_z = 79\%$ is held by the downward stress, which is then transferred to the base wall. Further analysis of the forces at the walls reveals that friction on the side walls is measured to be $t_x^l/t_z^l = 0.41$ for the left and $-t_x^r/t_z^r = 0.42$ for the right side wall.
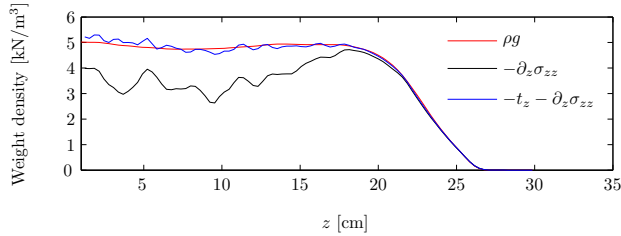
Figure 17: Components of the hydrostatic stress balance, eq (19): Weight density ρg_z, the downwards stress gradient $-\partial_z \sigma_{zz}$, and the combination of shear forces at the wall, $-t_z$, and the stress gradient. Data averaged over x, y and $1 \leq t \leq 1.4$ for $w = d$.

20

4.6. Flow rheology

Next, we take a look at the mobilised macroscopic friction, the ratio between shear stress and normal stress, evaluated as

$$\mu = \frac{1}{\sqrt{6}p}\sqrt{(\sigma_1 - \sigma_2)^2 + (\sigma_2 - \sigma_3)^2 + (\sigma_3 - \sigma_1)^2}, \tag{20}$$

where σ_i denotes the eigenvalues of the stress tensor and p the pressure. The macroscopic friction ranges from 0.7 to nearly 1 almost everywhere except near the flow surface, as shown in Figure 18a, which is consistent with the chosen microscopic interparticle sliding and rolling friction. It is particularly high in the shear zone, which is not surprising, as the friction in sheared (critical) flows is known to be a function of the inertial number, $I = \frac{\dot{\gamma}d}{\sqrt{p\rho_p}}$. This is shown in Figure 18b. While no clear functional behaviour can be seen, the friction is clearly increasing with inertial number.
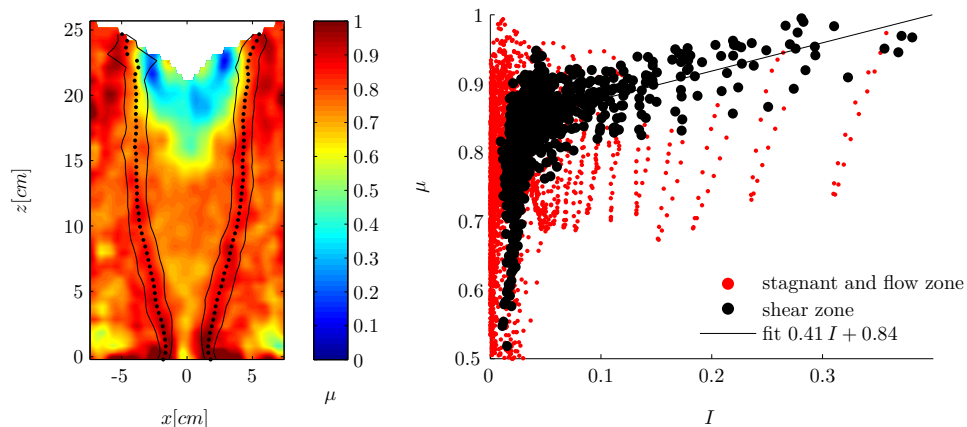
Figure 18: *Left*: Mobilised macroscopic friction $\mu = |\sigma^D|/p$ as function of position. Dots and lines denote the centre and width of the shear zone, respectively (according to (18)).*Right*: Friction as function of inertial number. The data from the shear zone data for $I > 0.1$ is fitted linearly. All data averaged over y and $1 \le t \le 1.4$ for $w = d$.

5. Conclusion

In this article, coarse-graining (CG) formulations (i.e. the micro-macro transition) are reviewed and applied to a simulation of the flow through a model

scale quasi-2D silo, as an example of a spatially inhomogeneous system. The system is homogeneous in depth y and, consequently, all variables are averaged over this direction. The remaining two-dimensional fields show three well defined regions, where a fast-flowing core is separated by a narrow shear band from a stagnant outer region. The temporal evolution of the system shows that the flow is fully developed in the interval $0.75\,\mathrm{s} < t < 2\,\mathrm{s}$, where most fields vary little over time except that the stresses decreases gradually over time due to the decreasing height of the solid.

The CG formulation depends on two parameters, the spatial and temporal averaging length scales w and Δt. To determine the optimal parameters, one point from each region is analysed for different parameter values. Time-averaging around the instant $t = 1.2\,\mathrm{s}$ shows that the variables are independent of the chosen time interval for $\Delta t < 1.2\,\mathrm{s}$. However, the variance of the (time-dependent) stress in the stagnant zone increases for $\Delta t > 0.4\,\mathrm{s}$; therefore, $\Delta t = 0.4\,\mathrm{s}$ is selected as the optimal time-averaging interval.

The results for the coarse-graining width w show that for $w/d < 0.5$, the averaged fields are strongly dependent on the choice of Δt for $\Delta t < 0.4\,\mathrm{s}$, indicating that the fluctuations in the data are too significant to obtain meaningful averages. For $0.5 < w/d < 1$, the resulting fields are nearly parameter-independent, therefore $w = d$ is recommended for spatial averaging.

The study shows that the choice of spatial coarse-graining width and time averaging interval is crucial to obtain meaningful field definitions in systems with highly localized behaviour. While no general choice of parameters is obtained, the article outlines how to obtain the ideal set of parameters for an individual system.

Once the CG parameters are selected, the macroscopic fields are used to study the flow patterns in the silo. To demarcate the three distinct flow regions, we look for a definition of the location and width of the shear bands. We observe that the tensorial shear rate $\dot{\gamma}$ and the inertial number are high in the left and right shear band (mainly simple shear) as well as in the core flow region (mainly pure shear). Thus, the horizontal shear rate, $\partial_x v_z$, is used to define the shear

band, as it almost vanishes in the core flow region.

We compare three definitions for the shear band centre and width at a given height z: *(a)* the maximum and the 0.6-quantile of the shear rate, *(b)* the centroid and hygroscopic radius of the shear rate, and *(c)* the mean and standard deviation of a Gaussian fit to all shear rate values above the 0.6-quantile. Definition *(c)* is recommended, as for definition *(a)* both width and centre are dependent on the spatial resolution upon which the fit is made, and the width is strongly parameter-dependent in both definitions *(a)* and *(b)*. Furthermore, the definition *(c)* of the width and centre are shown to be independent of w for $0.3 < w/d < 1$.

The stress analysis shows that the normal stresses are high in the stagnant region and nearly vanish in the flowing region. Furthermore, the normal stresses are highly anisotropic, with the downward stress much larger than the vertical stresses as would be expected in a silo condition [20, 21]. The stress is shown to transfer the weight of the flow to the walls, with the shear forces on the side walls carrying 21% and the base wall carrying 79% of the weight. Finally, the $\mu(I)$ rheology is addressed, which states that the ratio of shear and normal stresses, μ, is a function of the inertial number, I, if the flow is in critical steady state. This is shown to be true for the shear zone, where the friction increases nearly linearly with the inertial number [11, 22].

The analysis of the flow rheology in this paper is by no means complete, as the focus of this paper was to investigate and find the optimal CG parameters. In a further publication on this topic, we intend to analyse the stress tensor further to better understand the many interesting phenomena that can be observed in these situations. Examples are the strong stress anisotropy and the stick-slip behaviour near the walls, the rheology and the dynamic behaviour of the shear band, and the arch observed in the central flow region.

References

[1] S. Luding, F. Alonso-Marroquin, The critical-state yield stress (termination locus) of adhesive powders from a single numerical experiment, Granular Matter 13 (2) (2011) 109–119.

[2] J. H. Irving, J. G. Kirkwood, The statistical mechanical theory of transport processes .4. the equations of hydrodynamics, Journal of Chemical Physics 18 (6) (1950) 817–829.

[3] M. Born, K. Huang, Dynamical Theory of Crystal Lattices Oxford Classic Texts in the Physical Sciences, Clarendon Press, Oxford, 1988.

[4] B. D. Todd, D. J. Evans, P. J. Daivis, Pressure tensor for inhomogeneous fluids, Physical Review E 52 (2) (1995) 1627–1638.

[5] M. Babic, Average balance equations for granular materials, International Journal of Engineering Science 35 (5) (1997) 523–548.

[6] I. Goldhirsch, Stress, stress asymmetry and couple stress: from discrete particles to continuous fields, Granular Matter 12 (3) (2010) 239–252.

[7] D. Heyes, E. Smith, D. Dini, T. Zaki, The equivalence between volume averaging and method of planes definitions of the pressure tensor at a plane, Journal of chemical physics 135 (2) (2011) 024512.

[8] T. Weinhart, A. R. Thornton, S. Luding, O. Bokhove, Closure relations for shallow granular flows from particle simulations, Granular Matter 14 (4) (2012) 531–552.

[9] R. Hartkamp, A. Ghosh, T. Weinhart, S. Luding, A study of the anisotropy of stress in a fluid confined in a nanochannel, Journal of Chemical Physics 137 (4).

[10] C. Goldenberg, I. Goldhirsch, Effects of friction and disorder on the quasistatic response of granular solids to a localized force, Phys. Rev. E 77 (2008) 041303.

[11] T. Weinhart, R. Hartkamp, A. R. Thornton, S. Luding, Coarse-grained local and objective continuum description of three-dimensional granular flows down an inclined surface, Physics of Fluids 25 (7).

[12] T. Weinhart, A. Thornton, S. Luding, O. Bokhove, From discrete particles to continuum fields near a boundary, Granular Matter 14 (2) (2012) 289–294.

[13] J. Zhang, R. P. Behringer, I. Goldhirsch, Coarse-graining of a physical granular system, Progress of Theoretical Physics Supplement 184 (2010) 16–30.

[14] B. J. Glasser, I. Goldhirsch, Scale dependence, correlations, and fluctuations of stresses in rapid granular flows, Physics of Fluids 13 (2) (2001) 407–420.

[15] T. Weinhart, Accurate and efficient coarse-graining of particle data, Granular Matter (2014) in preparation.

[16] DEM Solutions, EDEM 2.5 User Guide, Tech. rep., Edinburgh, Scotland, UK (2014).

[17] DEM Solutions, EDEM 2.5 Hertz-Mindlin (no slip) with RVD Rolling Friction model, Tech. rep., Edinburgh, Scotland, UK (2014).

[18] C. Goldenberg, A. P. F. Atman, P. Claudin, G. Combe, I. Goldhirsch, Scale separation in granular packings: Stress plateaus and fluctuations, Physical Review Letters 96 (16).

[19] C. Labra, J. Y. Ooi, J. Sun, Spatial and temporal coarse-graining for DEM analysis, AIP Conference Proceedings 1542 (1) (2013) 1258–1261.

[20] J. Ooi, J. Rotter, Wall pressures in squat steel silos from simple finite element analysis, Computers and Structures 37 (4) (1990) 361–374.

[21] Y. Wang, Y. Lu, J. Ooi, A numerical study of wall pressure and granular flow in a flat-bottomed silo, Powder Technology (2015) [Accepted February 2015].

[22] GDR MiDi, On dense granular flows, The European Physical Journal E 14 (4) (2004) 341–365.